JOURNAL OF SYNCHROTRON RADIATION

ISSN 1600-5775

Comparative analysis of sample preparation protocols of soft biological tissues for morphometric studies using synchrotron-based X-ray microtomography

Carlos Sato Baraldi Dias,[a]* Dionísio Pedro Amorim Neto,[b] Giovanni Lenzi Baraldi[a] and Matheus de Castro Fonseca[b]*

[a]Brazilian Synchrotron Light National Laboratory, Brazilian Center for Research in Energy and Materials (CNPEM), Giuseppe Maximo Scolfaro 10000, Campinas, São Paulo 13083-970, Brazil, and [b]Brazilian Biosciences National Laboratory, Brazilian Center for Research in Energy and Materials (CNPEM), Giuseppe Maximo Scolfaro 10000, Campinas, São Paulo 13083-970, Brazil. *Correspondence e-mail: carlos.sato@lnls.br, matheus.fonseca@lnbio.cnpem.br

Received 8 March 2019
Accepted 13 August 2019

Edited by Y. Amemiya, University of Tokyo, Japan

Keywords: microtomography; soft tissues mounting; synchrotron radiation.

Supporting information: this article has supporting information at journals.iucr.org/s

The spread of microtomography as a tool for visualization of soft tissues has had a significant impact on a better understanding of complex biological systems. This technique allows a detailed three-dimensional quantitative view of the specimen to be obtained, correlating its morphological organization with its function, providing valuable insights on the functionality of the tissue. Regularly overlooked, but of great importance, proper sample mounting and preparation are fundamental for achieving the highest possible image quality even for the high-resolution imaging systems currently under development. Here, a quantitative analysis compares some of the most common sample-mounting strategies used for synchrotron-based X-ray microtomography of soft tissues: alcoholic-immersion, paraffin-embedding and critical-point drying. These three distinct sample-mounting strategies were performed on the same specimen in order to investigate their impact on sample morphology regardless of individual sample variation. In that sense, the alcoholic-immersion strategy, although causing less shrinkage to the tissue, proved to be the most unsuitable approach for a high-throughput high-resolution imaging experiment due to sample drifting. Also, critical-point drying may present some interesting advantages regarding image quality but is also incompatible with a high-throughput experiment. Lastly, paraffin-embedding is shown to be the most suitable strategy for current soft tissue microtomography experiments. Such detailed analysis of biological sample-mounting strategies for synchrotron-based X-ray microtomography are expected to offer valuable insights on the best approach for using this technique for 3D imaging of soft tissues and following morphometric analysis.

1. Introduction

The three-dimensional (3D) morphology and function of biological structures carry a strong correlation, and thus the development and usage of imaging techniques contributes to the understanding of most biological systems. So far, the methods used for constructing 3D visualizations of biological specimens down to cellular resolution have fallen into two categories: those based on reconstruction from serial-sectioned images and those based on whole-volume imaging. Within this context, the use of optic light microscopy for biological imaging is historically bound to two-dimensional (2D) images (Shearer *et al.*, 2016) that when stacked from serialized slices can form a complete 3D image of the desired structure. However, this approach is technically challenging, time-consuming and mainly limited by the sample volume and

size, that in many cases leads to the introduction of substantial structural artifacts to the reconstructed image. On the other hand, the constant development of X-ray tomography has opened the possibility for whole-volume imaging down to cellular resolution, with no theoretical limitation on sample size and volume (Metscher, 2009), allowing for a much more robust and reproductive 3D imaging.

With the development of brighter X-ray synchrotron sources and the creation of a new branch of X-ray microscopy named microtomography (μCT), biologists are now able to determine the 3D structure of different kinds of biological samples (Chen *et al.*, 2009; Fusseis *et al.*, 2009; Zhu *et al.*, 2011) at the micrometre down to submicrometre level (Bonse & Busch, 1996; Salomé *et al.*, 1999; Mizutani & Suzuki, 2012). Examples of X-ray μCT include the 3D imaging of many species of organisms including human (Bonse & Busch, 1996; Salomé *et al.*, 1999; Mizutani *et al.*, 2008), mouse (Johnson *et al.*, 2006; de Crespigny *et al.*, 2008; Mizutani *et al.*, 2010; Fonseca *et al.*, 2018) and insect (Mizutani *et al.*, 2007; Metscher, 2009; van de Kamp *et al.*, 2011). It has also become a valuable method in research focused on osteo and dental microstructures (Neues & Epple, 2008; Zou *et al.*, 2011).

When it comes to soft structures – typically the main component of biological tissues – solid sample preparation and appropriate contrast agent are necessary for whole-mount imaging with the aim to avoid sample artifacts and to provide detailed visualization of the biological structures of interest. Indeed, most unstained soft biological tissues exhibit an almost uniform density in a conventional X-ray image, allowing for some contrast only at the outline of the soft tissue but not of their internal constituents, including individual cells (Mizutani & Suzuki, 2012).

Pursuing an adequate contrast for biological samples was crucial for optical microscopy, and the case is similar for X-ray microscopy with similar demands for appropriate contrast enhance reagents when pursuing high-resolution images (Metscher, 2009). However, for high-resolution 3D microtomography of a biological sample, an additional factor should be addressed during sample preparation. Data collection by synchrotron-based X-ray microtomography is performed by rotating the sample on a stage and taking multiple X-ray projection images from different angles while the source and detector are kept static. The acquired projections are then fed into a reconstruction algorithm, such as the well established Filtered Back-Projection (FBP), that back-propagates the projections into the original volume. Such algorithm assumes that the sample itself does not move except for a rotation around a well established axis during the entire data acquisition. As such, any sample movement, apart from the rotation, will break the consistency between the projections leading to a decreased resolution of the final reconstruction.

Furthermore, when it comes to soft tissues, it should also be considered that the sample suffers deformation or drift during scanning, while ideally it should be rigid during the entire acquisition. Although those deviations at the projection could be modeled and incorporated in the reconstruction algorithm (Miqueles *et al.*, 2018), proper offline sample preparation is a much more robust strategy to achieve high-resolution imaging and minimize the possible artifacts linked to the sample motion (Kak & Slaney, 1988). Therefore, to visualize thin delicate structures of soft tissues by using synchrotron radiation sources and obtain high-resolution images, tissue samples should be prepared by accordingly considering several variables that might interfere with image quality. One important factor is proper offline sample mounting.

In this work, we compare three mounting strategies of biological samples found in the literature (Metscher, 2009; Mizutani & Suzuki, 2012) that are compatible with synchrotron microtomography, discussing their impact on image quality and sample morphology. We tested multiple sample preparation protocols on the same zebrafish larva and tracked its changes in morphology due to the offline sample preparation. We performed high-resolution synchrotron microtomography as the specimen gradually progressed from initial ethanol dehydration, used for sample preservation, and isopropanol immersed; passing from paraffin embedding, used for histology; until being completely dried by critical-point drying, used for scanning electron microscopy. Finally, we were able to segment the specimen and perform a digital histological analysis quantifying the volume of inner structures such as the heart and eyes, as an example of the capabilities of the technique.

2. Materials and methods

2.1. Specimen used

For this study, 48 h post-fertilization (48hpf) wild-type zebrafish (*Danio rerio*) larvae were used. Adults and larvae were maintained in a zebrafish housing system (LNBio, CNPEM, Brazil). Fish were fed twice a day with a commercial flake food (Tetra, Daleville, VA, USA) and with live brine shrimp to incite optimal egg production. Newly fertilized eggs were raised at 28°C in embryo water (Milli-Q water with 60 mg ml^{-1} Instant Ocean), and larvae collected after 48 h. Experimental protocols were carried out in strict accordance with the recommendations outlined in the Guide for the Care and Use of Laboratory Animals of the Brazilian National Council of Animal Experimentation (http://www.cobea.org.br/) and the Federal Law 11.794 (8 October 2008). The Institutional Committee for Animal Ethics of the Brazilian Center for Research in Energy and Materials (CEUA-CNPEM) approved all the procedures used in this study.

2.2. Sample preparation and mounting strategies

48hpf larvae (N = 4) were collected and immediately immersed in ice-cold fixative modified Karnovsky solution. Specimens were maintained in a fixative solution overnight at 4°C. After fixation, samples were washed with cacodylate buffer (0.1 M) and post-fixed in reduced osmium (1% osmium tetroxide) for 30 min (Rodrigues *et al.*, 2013). Next, samples were washed with cacodylate buffer, dehydrated through ascending series of ethanol solution (70, 80, 90, 95 and 100%), bathed for 30 min in 100% isopropanol and placed into a

5 mm glass capillary filled with 100% isopropanol. After microtomography, samples were cleared in xylol (two baths of 15 min each) and embedded in Paraplast Plus (Sigma Aldrich, St Louis, MO, USA). Following a second round of imaging, samples were immersed in xylol to remove the embedding medium, and then bathed in 100% acetone (1 h) for critical-point drying. Samples were critical-point-dried by flooding with liquid carbon dioxide at 5°C for 20 min and then raising the temperature to the critical point. For best results, samples were dehydrated twice followed by 100% acetone washing before critical-point drying. In order to exclude the inherent radiation damage during multiple scanning of the same sample from the morphological analysis, another group of samples (N = 4 for each condition) were submitted to only one of the mounting procedures mentioned and scanned once.

2.3. IMX beamline setup (UVX-LNLS) and 3D reconstruction

The stained samples were mounted on a stub on the rotation stage [Fig. 1(*b*)]. More than 2000 X-ray projection images were acquired by revolving the sample around a fixed rotation axis by 180°, in uniformly spaced angular steps, to produce a stack of sinograms that were later computationally converted into a 3D map of the electron density of the sample, as previously described (Fonseca *et al.*, 2018). The transmission images were obtained using radiation from the 1.67 T bending magnet of the 1.37 GeV UVX storage ring, filtered by 0.9 mm or 0.2 mm Si filters. These setups generated a polychromatic beam, with peak energy at approximately 15 keV or 11 keV, respectively, and approximately 50% bandwidth. The radiographs were recorded by an indirect detector system, based on a 50 µm-thick LuAG:Ce scintillator that transforms the transmitted X-rays into visible light. The light is focused on a PCO2000 CCD sensor by an infinity-corrected optics, which can produce an adjustable magnification of the visible-light image radiating from the scintillator, yielding X-ray projection images with a final pixel size of 0.82 µm × 0.82 µm. Considering the array size of 2048 × 2048 of the PCO2000 CCD, the field of view (FOV) of the radiographs was 1.7 mm × 1.7 mm for the high-resolution images. A total of 2048 projections and an exposure time of 1 s per projection were used to compose the dataset for image reconstruction using the BST approach

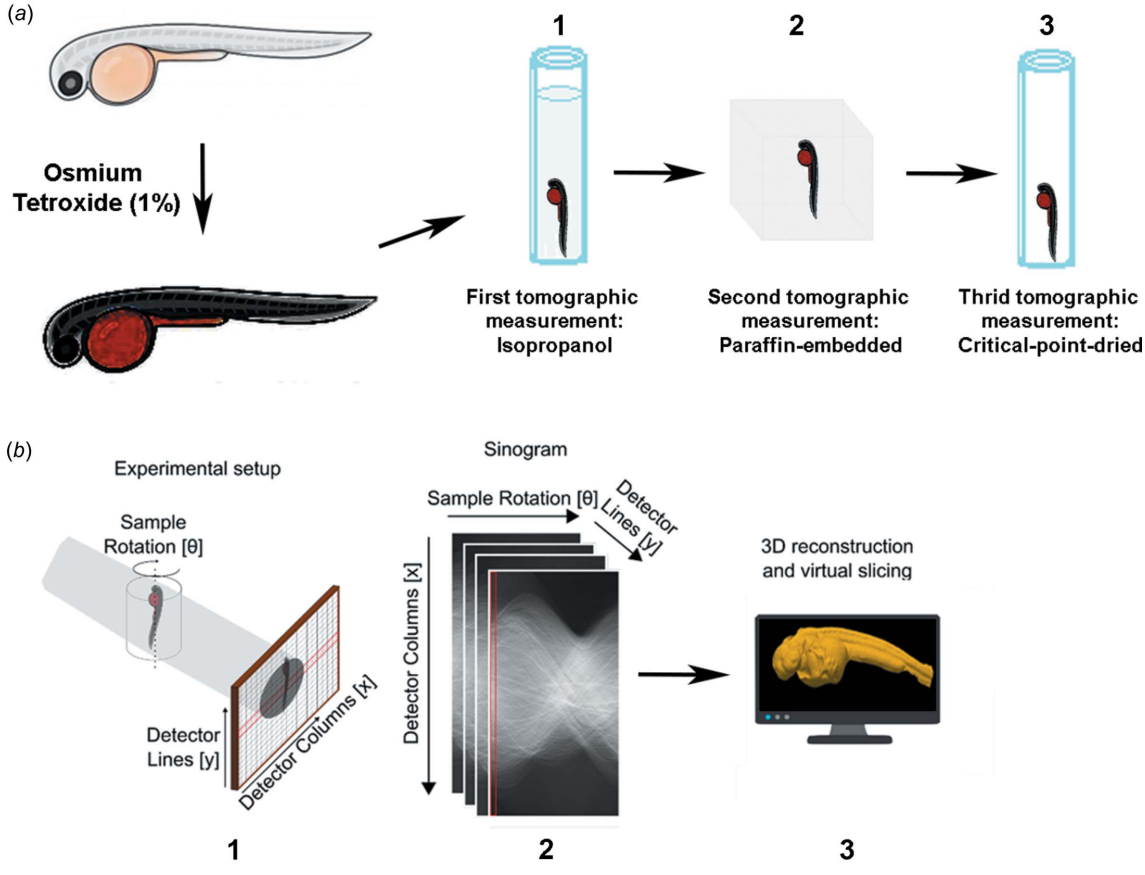

Figure 1
Schematic illustration of the experimental procedures and beamline setup. 48hpf zebrafish larvae were collected, fixed and immersed into 1% osmium tetroxide solution for 30 min. Then, samples were washed in 1% cacodylate solution. Next, samples were dehydrated, washed with cacodylate buffer, bathed for 30 min in 100% isopropanol and placed into a 1 mm glass capillary filled with 100% isopropanol (1). After microtomography, samples were dehydrated through ascending series of ethanol solution, cleared in xylol (two baths of 15 min each) and embedded in Paraplast Plus. Following a second microtomography (2), samples were immersed in xylol to remove the embedding medium, and then bathed in 100% acetone (1 h) for critical-point drying and measured for the third time (3). (*b*) Schematic view of the experimental setup for synchrotron-based X-ray microtomography. (1) X-rays from a synchrotron bending-magnet source illuminated the samples positioned in front of an indirect X-ray detector. (2) Projection images, acquired by a rotational scan, were used to reconstruct the tomographic slices (3).

Table 1
Parameters for the data acquisition condition.

The IMX beamline setup was used for data acquisition.

Beamline	IMX
X-ray energy (keV)	Pink beam (11 keV)
Rotations per frame (°)	0.17
Exposure per frame (ms)	1000
Frames per data set	2048
Data set acquisition time (min)	40
Pixel size (µm)	0.82
Instrumental resolution (µm)	1.62
Viewing field (mm)	1.7 × 1.7

(Fonseca *et al.*, 2018). All the data acquisition conditions are summarized in Table 1. Data were reconstructed using the standard backprojection approach (Miqueles *et al.*, 2018; Koshev *et al.*, 2016), available as part of the software *RAFT* (Miqueles & De Pierro, 2011).

2.4. Data processing

3D reconstructed data obtained at the IMX beamline were post-processed using the free Fiji software *ImageJ* with Trainable Weka Segmentation and MorphoLibJ plugins (Legland *et al.*, 2016). The segmented image of the zebrafish was visualized and analyzed using *Avizo* software as in our previous work (Fonseca *et al.*, 2018).

3D reconstructions were first analyzed using the Weka plugin from Fiji that provided a labeled result based on the training of a classifier for separating the sample from the background and any sample holder structure. The result was a binary mask excluding most of the background and thus digitally isolating the sample. Afterwards, the obtained binary mask was inspected and the segmented region was refined using the mathematical morphology methods available in the MorphLibj plugin. Furthermore, it is worth noting that the trained classifier was the same for all the samples in the same group, and the post-processing followed the same criteria for all the samples in the experiment.

After segmentation of the entire specimen, the 3D model was digitally sectioned immediately below the anal pore as a normalization for comparison of equivalent volumes and lengths between specimens. The quantitative analysis of each specimen was performed using the software *Avizo* together with 3D rendering.

For internal structure segmentation of the heart and eyes, including retina and lens, a laptop with a touchscreen and stylus pen for freehand selection on a remote desktop with *Avizo* software was used. Finally, the structure contour at different slices was further interpolated into a whole volume.

The Weka segmentation methodology used in this manuscript can be easily adapted to any other type of image, including 2D. However, the final refinement depends on the reconstruction algorithm and experimental setup, and so adjustments might be necessary for proper segmentation.

2.5. Statistics and Fourier shell correlation

Quantitative results are expressed as mean ± standard deviation. GraphPad *Prism* 6.0 (GraphPad, La Jolla, CA, USA) was used for data analysis. Groups of data were compared by Student's t-test, and a p-value of <0.05 was taken to indicate statistical significance.

Fourier shell correlation (FSC) calculations (van Heel & Schatz, 2005) were carried out using sub-volumes extracted from the unsegmented image comprising only the region of the larvae and excluding background.

3. Results

In our current setup, microtomographic visualization of X-ray absorption images takes from a few minutes to a couple of hours. On the other hand, much more time is needed to obtain phase-contrast images (Mizutani & Suzuki, 2012). When it comes to soft tissues, such as those presented in biological specimens, sample deformation or drifting faster than the acquisition time might cause undesired artifacts in the final resultant tomogram. Also, for comparative morphological analysis of biological specimens, sample shrinking due to either radiation damage or the chosen sample preparation protocol must be addressed to avoid misinterpretation of the data.

In order to evaluate the effects of different sample-mounting protocols on the morphology of soft tissues and the quality of the microtomogram obtained, we submitted 48hpf zebrafish to common strategies of sample mounting used to avoid sample drifting or deformation during synchrotron-based X-ray microtomography acquisition.

The most usual form of preserving biological structures is by paraformaldehyde prefixed-dehydration, keeping the specimen immersed in ethanol, making this one of the most common practices for 3D imaging. In this study, after fixation, samples were contrasted using osmium tetroxide to allow better visualization of inner structures.

After fixation, the 48hpf larvae were submitted to mounting in liquid isopropanol, paraffin embedding or critical-point drying, as shown in Fig. 1(*a*). It is important to mention that the same sample was submitted for all of these conditions, with imaging at each point so that we could observe the morphological alteration throughout these procedures on individualized larvae. Fig. 1(*b*) shows an overview of the experimental setup used at the synchrotron (UVX-LNLS, Brazil) beamline for X-ray microtomography (IMX). The sample was positioned and rotated at a distance of 40 mm from the detector which had an adjustable pixel size of 0.82 µm for high-resolution/small-FOV imaging. All image acquisition and setup details are given in Section 2. Reconstructed virtual slices were subsequently segmented and analyzed.

Fig. 2(*a*) shows representative images of a segmented larva after different sample-mounting conditions. It can be observed that the isopropanol-immersed larva has a significantly decreased length and volume after being submitted to paraffin embedding. However, when the same sample was removed

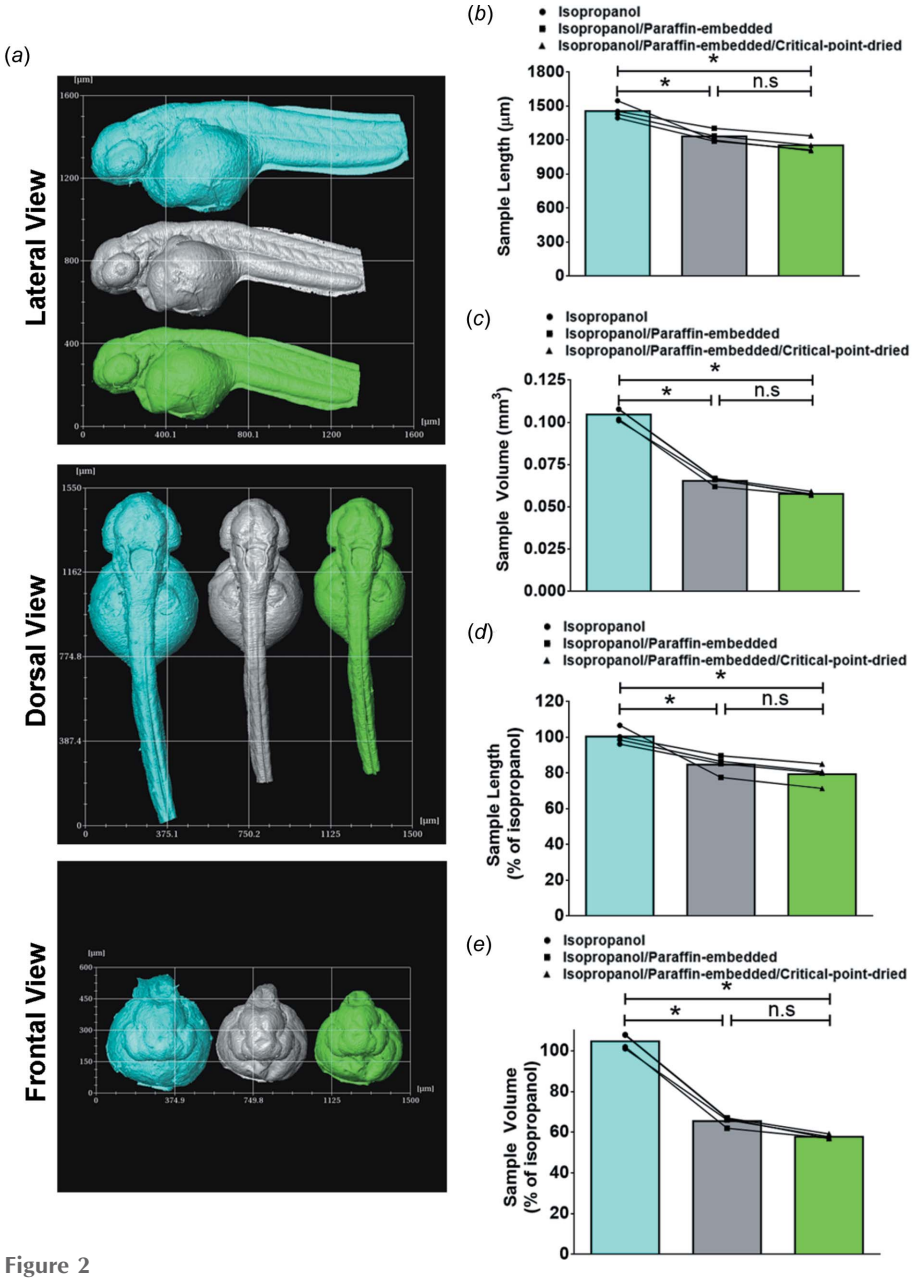

Figure 2
3D reconstructed volumes of µCT data of 48hpf zebrafish for three different conditions of sample mounting. (*a*) Lateral, dorsal and frontal view of a single 48hpf zebrafish mounted in liquid isopropanol (blue), paraffin-embedded (gray) and critical-point-dried (green). The bar graph shows the reduction in sample length (*b*) and volume (*c*) as it proceeds along the experimental pipeline shown in Fig. 1. Graphs (*d*) and (*e*) show the reduction in total sample length (*c*) and volume (*d*) plotted as a percentage of the isopropanol condition (first sample-mounting strategy). In all graphs, lines connect individual samples to show individual alteration throughout the procedure. Values indicate the mean ± standard deviation. $^*P < 0.05$: the difference between groups was statistically significant; ns: not significant. Data were analyzed by one-way ANOVA followed by Bonferroni post-tests. $N = 4$ samples. Scale ($X \times Y$): lateral view: 1600 µm × 1600 µm; dorsal view: 1500 µm × 1550 µm; frontal view: 1500 µm × 600 µm.

from paraffin and critical-point-dried, no significant reduction was detected [Figs. 2(*b*)–2(*e*)]. A precise quantification is shown in Figs. 2(*b*)–2(*e*) and Table 2. In order to confirm whether such morphological changes are due to the sample-mounting procedure alone instead of radiation damage during measurements or excessive sample manipulation, 48hpf independent larvae were separately submitted to either isopropanol immersion, paraffin embedding or critical-point drying. Morphometric analysis showed that the same shrinking was observed, confirming that sample mounting definitely alters sample morphology in a statistically significant manner independently of possible radiation damage or excessive manipulation (see Fig. S1 and Table S1 of the supporting information).

Detailed morphological visualization of soft tissues at the micrometre scale is essential for comparative, functional and developmental biology (Ruffins *et al.*, 2007; Fonseca *et al.*, 2018; Smith *et al.*, 2009). However, the inner structures of an organism are especially susceptible to deformations during sample preparation or image acquisition. In order to analyze the possible alteration on such structures, we segmented the retina, lens and heart of 48hpf zebrafish that were submitted to the three sample-mounting approaches. When we analyzed retina and lens volume, both structures followed the same pattern of shrinking, being the more striking alteration observed when samples were submitted to paraffin embedding, leading to a reduction of around 40% in volume when compared with isopropanol (Fig. 3 and Table 3). Owing to the presence of empty spaces corresponding to the heart cavities, the alteration observed in this organ was even more pronounced, showing a reduction of around 60% when compared with the samples measured in isopropanol (Fig. 4 and Table 3). Similar to for the retina and lens, the pattern of shrinking observed for the heart was also more prominent with the paraffin-embedding mounting strategy [Figs. 4(*b*)–4(*c*); Table 3]. Also, for all the structures analyzed, no statistically significant differences were observed between the paraffin-embedding and critical-point-drying approaches.

It is worth noting that, although the decrease in sample volume depends on the mounting strategy chosen, the inner structures analyzed are also submitted to the same alteration having their volume/total sample volume ratio maintained throughout the measures [Figs. 3(*c*) and 4(*c*); Table 4].

In order to compare the obtained reconstruction of each sample-mounting condition, we selected one *z*-slice of the

Table 2
Morphometric analysis of whole larvae after being serially submitted to each sample-mounting condition and μCT.

Values (raw values and plotted as a percentage of isopropanol condition) show the reduction in sample length (μm) and volume (mm^3) as the experimental pipeline proceeds.

	Isopropanol	Isopropanol/ paraffin-embedded	Isopropanol/ paraffin-embedded/ critical-point-dried
Length	1457.25 ± 32.58 (100.50 ± 2.24%)	1234.75 ± 25.81 (84.79 ± 2.57%)	1153.75 ± 30.24 (79.31 ± 2.86%)
Volume	0.10 ± 0.001 (104.70 ± 1.84%)	0.06 ± 0.001 (65.45 ± 1.16%)	0.05 ± 0.001 (61.75 ± 0.51%)

Table 3
Values of lens, retina and heart volumes of 48hpf zebrafish larvae after being serially submitted to each sample-mounting procedure.

Values (raw values and plotted as percentage of isopropanol condition) show the reduction in the structure volume (mm^3) as the experimental pipeline proceeds.

	Isopropanol	Isopropanol/ paraffin-embedded	Isopropanol/ paraffin-embedded/ critical-point-dried
Lens	0.00014 ± 0.00001 (95.14 ± 9.80%)	0.00010 ± 0.00001 (66.56 ± 7.82%)	0.00008 ± 0.00001 (62.51 ± 5.84%)
Retina	0.0014 ± 0.0001 (95.14 ± 9.80%)	0.00098 ± 0.00017 (66.56 ± 7.82%)	0.00093 ± 0.0001 (59.37 ± 6.85%)
Heart	0.0003 ± 0.00003 (100.1 ± 8.70%)	0.0001 ± 0.00002 (52.61 ± 7.10%)	0.0001 ± 0.00002 (47.16 ± 6.10%)

same region of the head and the heart of the 48hpf zebrafish larvae and carefully analyzed the image quality and resolution, following the FSC 1/2-bit criteria (van Heel & Schatz, 2005). A reduction in area and also some alteration on the morphology of some delicate structures such as the larva heart (marked with H) can be seen in Fig. 5(*a*). Also, the *z*-slice obtained from the critical-point-dried sample-mounting strategy shows sharper features when compared with the *z*-slice of the other mounting strategies. As can be seen, the limits between two individual cells are more evident with this strategy. With the aim to quantify image resolution for the evaluated case, Fig. 5(*b*) shows the FSC for the respective reconstructed volumes. Although presenting a reduced image quality, isopropanol-immersed larvae have a better FSC-calculated resolution: 2.4 μm compared with 2.6 μm for the paraffin-embedded and the critical-point-dried condition and 3.0 μm for the critical-point-dried sample.

4. Discussion

Much progress in synchrotron radiation microtomography (μCT) and nanotomography (nano-CT) has been made in the past years. These advances resulted in visualizations of 3D structures at resolutions below 100 nm (Andrews *et al.*, 2010; Wang *et al.*, 2011). Also, microtomographic studies of soft tissues, which account for a considerable proportion of biological samples, have shed light on the structural mechanisms of biological functions (Happel *et al.*, 2010; Mizutani *et al.*, 2010). Although well established imaging methods such as magnetic resonance (Dorr *et al.*, 2008), serial block-face electron microscopy (Mikula *et al.*, 2012) and histological sectioning (Amunts *et al.*, 2013) are frequently used for morphometric analysis, they still face some issues such as lack of contrast, sample opacity limitation, time-consuming sample preparation protocols and the destructive nature of serial sectioning. Therefore, a nondestructive method such as synchrotron-based X-ray microtomography is a natural candidate for 3D volume imaging of biological samples. Notably, the 3D data generated by μCT can be segmented and interrogated to provide not only valuable qualitative visual data but also quantitative measurements of, for example, cell number, volume of organs, abundance of extracellular matrix porosity *etc.* (Shearer *et al.*, 2016; Keyes *et al.*, 2013; Fonseca *et al.*, 2018; Mizutani *et al.*, 2007). Recently, considerable advances in μCT technology have been made, now allowing sub-micrometre resolution, capture of phase-contrast information and faster tomograms acquisition, including improvements in sample preparation and imaging protocols (Bravin *et al.*, 2013; Scherer *et al.*, 2014; Balint *et al.*, 2016). Data collection in X-ray μCT is performed by rotating the sample while taking X-ray images at different angles. In order to allow a proper reconstruction, the sample should rotate exactly following the rotation of the sample stage. If the sample drifts or deforms faster than the necessary acquisition time, artifacts will be present in the resultant microtomography. Thereby, proper sample preparation and mounting are critical points in order to rule out these issues. During sample preparation, for example, different fixatives and contrast agents can be used for μCT imaging of soft tissues (Vickerton *et al.*, 2013; Sombke *et al.*, 2015; Pauwels *et al.*, 2013; Metscher, 2009). However, it is important to mention that pretreatment of biological samples to be imaged might alter their original morphological features. A general protocol is the fixation of biological samples with formalin and contrasted with osmium tetroxide, one of the most commonly used contrast agents (Johnson *et al.*, 2006; Bentley *et al.*, 2007). Although formalin fixation is known to induce tissue shrinkage, it has been shown that such an artifact is relatively homogeneous and can, therefore, be corrected for (Weibel & Vidone, 1961; Scott *et al.*, 2015).

Of great importance during sample preparation, but often overlooked, is the sample-mounting procedure for which, nowadays, there are several approaches such as capillary embedding, resin embedding, paraffin embedding, critical-point drying or even alcoholic immersion. All of these approaches offer some pros and cons.

4.1. Biological sample mounting and acquisition challenges on microtomography

Immersion of a prefixed and dehydrated biological sample in a glass capillary filled with isopropanol is the most convenient and most straightforward strategy among the presented sample-mounting approaches used here. First, the glass capillary has comparatively low X-ray attenuation and very thin walls and diameter that allows the sample to rest stably

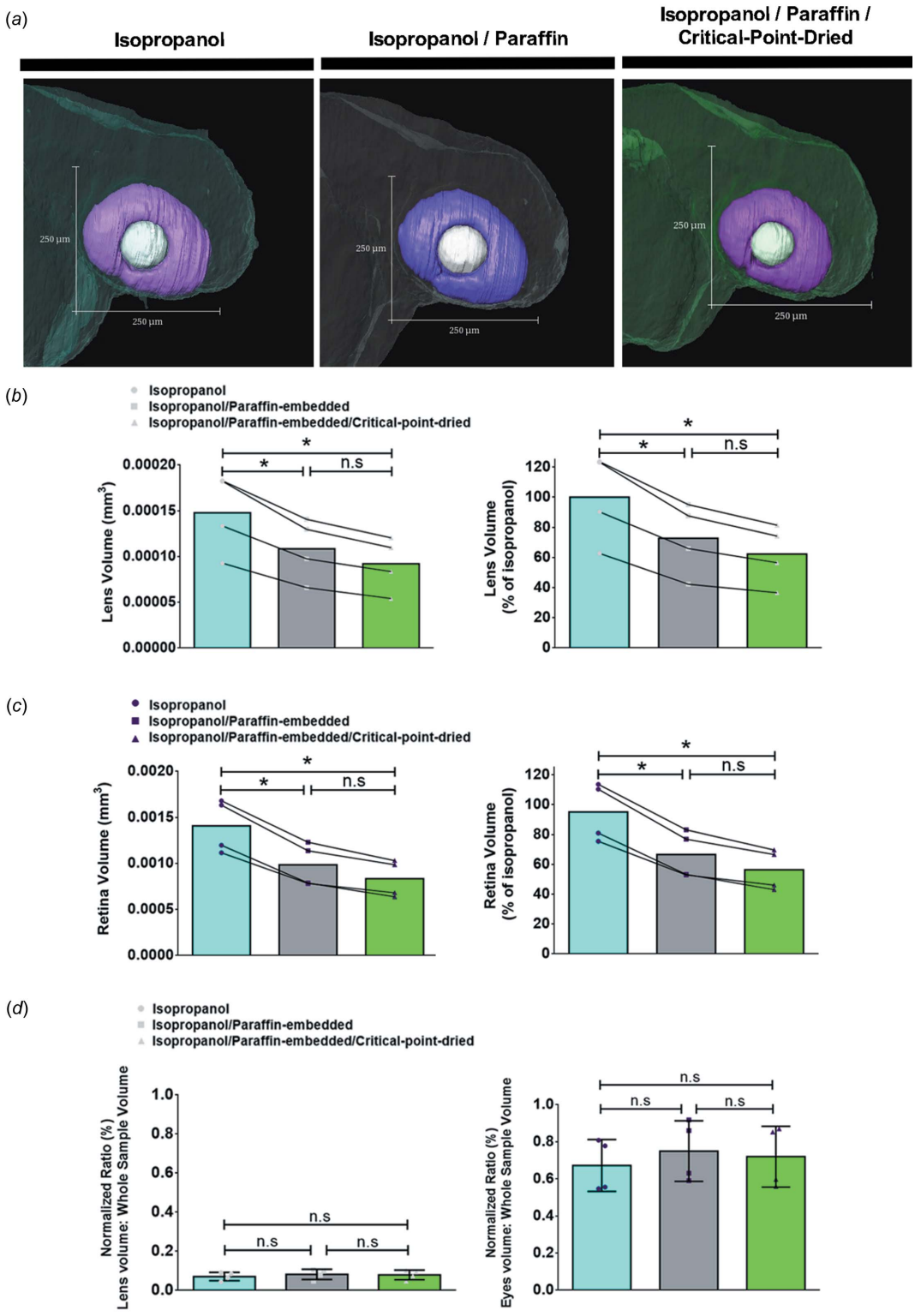

Figure 3
Segmentation followed by morphological analyses of the lens and retina volume of 48hpf zebrafish larvae after being serially submitted to each sample-mounting condition. (*a*) 3D views of an eye of a single segmented 48hpf zebrafish larvae imaged after each sample-mounting condition. The lens is digitally segmented in light gray and the retina in purple. (*b*) The left-hand bar graph show a more expressive reduction in lens volume after paraffin embedding and the right-hand graph exhibits the reduction in total lens volume plotted as a percentage of the isopropanol condition (first sample-mounting strategy). (*c*) The left-hand bar graph shows a more expressive reduction in retina volume after paraffin embedding and the right-hand graph exhibits the reduction in total retina volumes plotted as a percentage of the isopropanol condition (first sample-mounting strategy). (*d*) The left-hand graph presents the normalized ratio (%) of lens volume/whole sample volume. The right-hand graph presents the normalized ratio (%) of retina volume/whole sample volume. Where presented, lines connect individual samples to show the individual alteration throughout the procedure. Values indicate the mean ± standard deviation. $^*P < 0.05$: the difference between groups was statistically significant; ns: not significant. Data were analyzed by one-way ANOVA followed by Bonferroni post-tests. $N = 4$ samples. Scale ($X \times Y$): 250 µm × 250 µm.

Table 4
Normalized ratio (%) of lens, retina and heart volume per whole sample volume.

Values are plotted as a percentage of the isopropanol condition.

	Isopropanol	Isopropanol/ paraffin-embedded	Isopropanol/ paraffin-embedded/ critical-point-dried
Lens	0.07 ± 0.01%	0.08 ± 0.01%	0.07 ± 0.01%
Retina	0.67 ± 0.07%	0.75 ± 0.08%	0.71 ± 0.08%
Heart	0.34 ± 0.02%	0.28 ± 0.03%	0.29 ± 0.03%

with a minimum amount of medium surrounding it. Besides, the usage of absolute alcohol, such as isopropanol, gives better tissue contrast than water, as previously shown. Also, alcohols have the added advantage of holding fewer bubbles due to lower surface tension (Metscher, 2009; Fidalgo *et al.*, 2018). Such a crucial detail must be considered since air bubbles might cause the sample to drift during the acquisition, leading to an improper final reconstruction. The formation of gas bubbles is even more frequent for samples immersed in

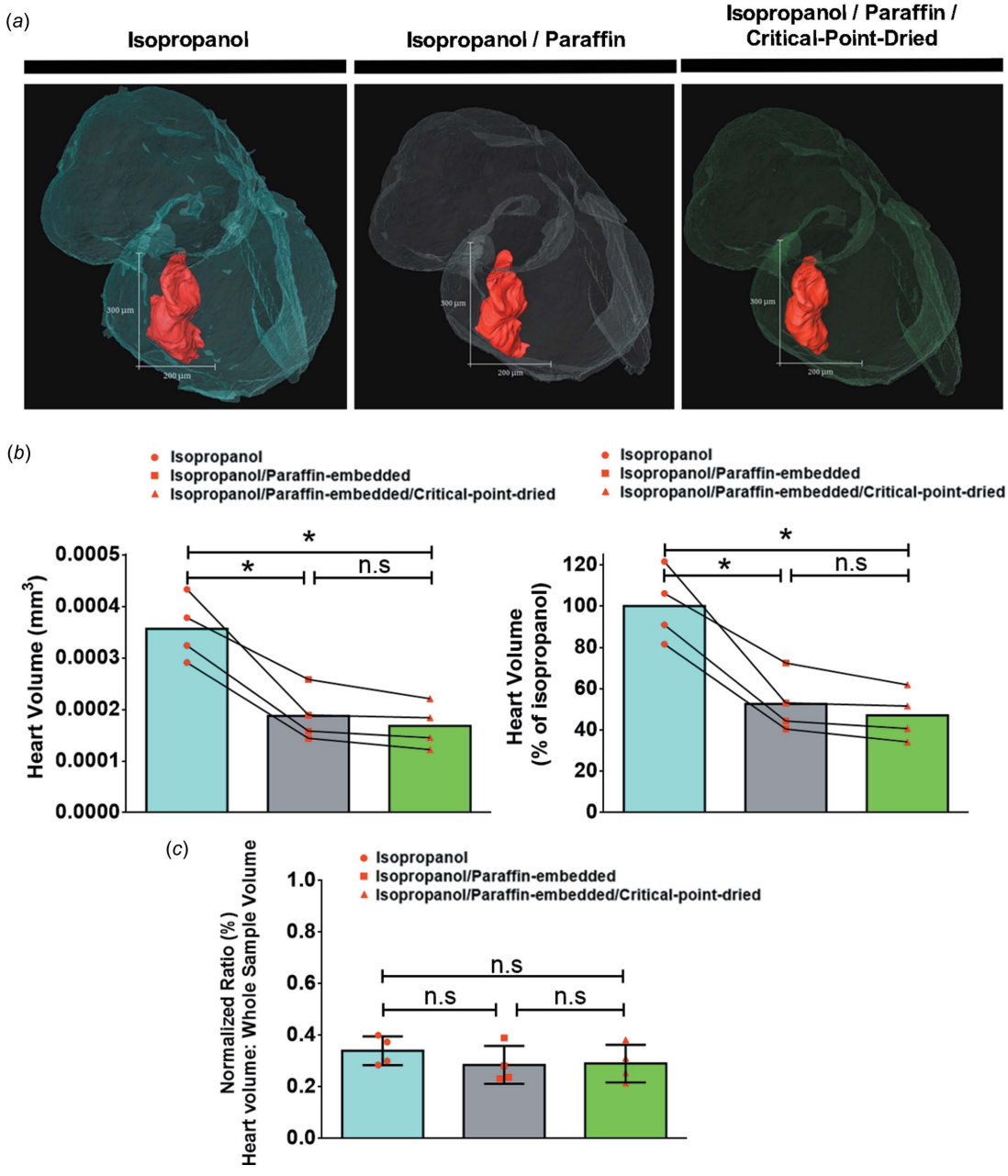

Figure 4
Morphological analyses of segmented heart volumes of 48hpf zebrafish larvae after being submitted to each sample-mounting condition (*a*) 3D views of the heart of a single segmented 48hpf zebrafish larvae imaged after each sample-mounting condition. The organ is digitally segmented in red. (*b*) The left-hand bar graph shows a more expressive reduction in heart volume after paraffin embedding and the right-hand graph shows the reduction in total heart volume plotted as a percentage of the isopropanol condition (first sample-mounting strategy). (*c*) Normalized ratio (%) of heart volume/whole sample volume. Where presented, lines connect individual samples to shown individual alteration throughout the procedure. Values indicate the mean ± standard deviation. $*P < 0.05$: the difference between groups was statistically significant; ns: not significant. Data were analyzed by one-way ANOVA followed by Bonferroni post-tests. $N = 4$ samples. Scale ($X \times Y$): 200 µm × 300 µm.

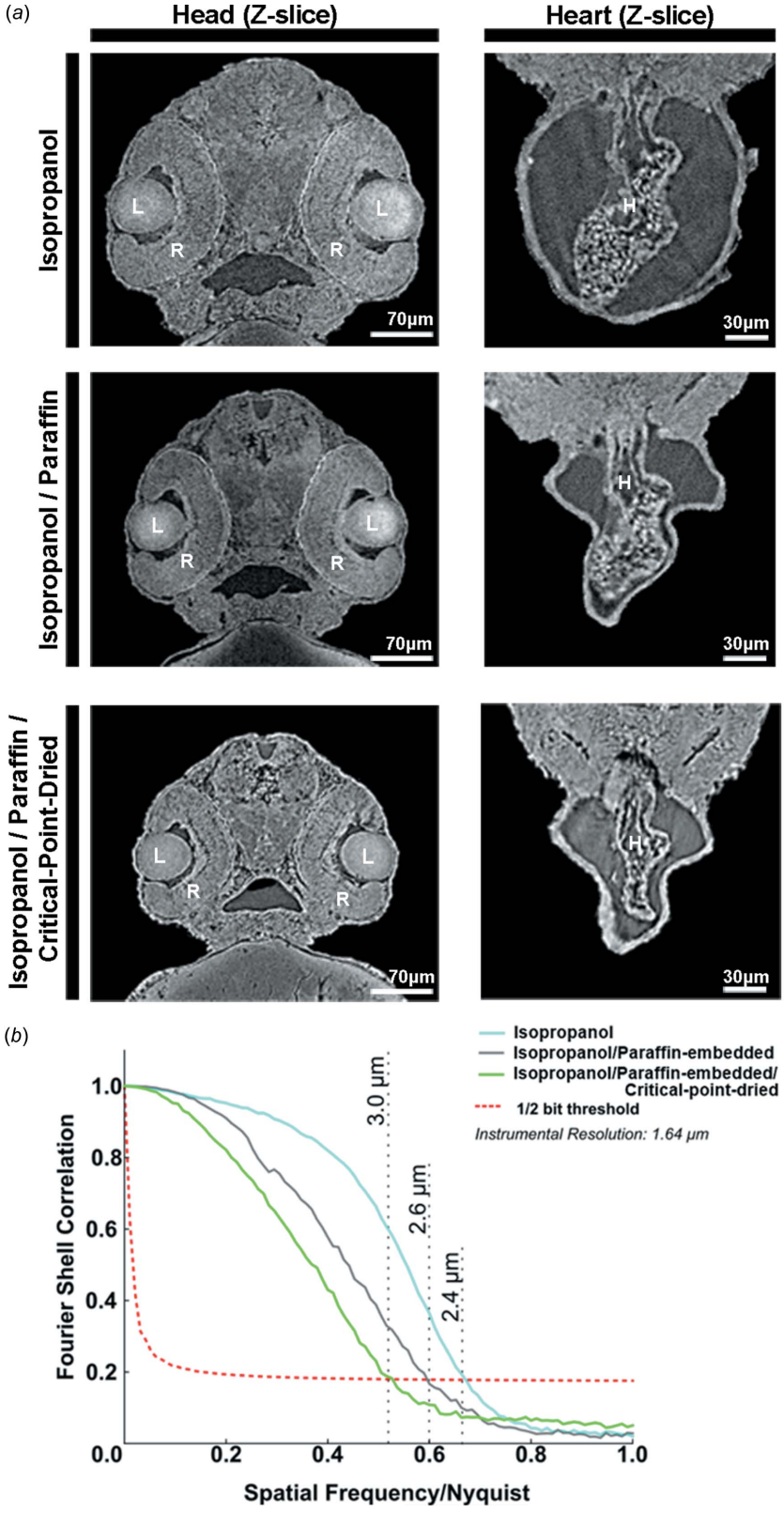

Figure 5
Tomographic slices and FSC of the same 48hpf zebrafish larva for each sample-mounting procedure. (*a*) *Z*-slice from the same larva imaged in isopropanol (top panel), paraffin embedding (middle panel) and critical-point dried (bottom panel). Observe the better image quality shown by single cell limits on a representative *z*-slice for the critical-point-dried procedure. Letters indicate the following structures: L, lens; R, retina; H, heart. (*b*) FSC showing a crescent image resolution: isopropanol > isopropanol/paraffin > isopropanol/paraffin/critical-point dried. The tilt angle ranges from 0° to 180°.

aqueous buffer solutions, making impractical any attempt to measure fresh samples at the IMX beamline (data not shown).

While the usage of isopropanol may mitigate the problem of bubble formation during image acquisition of samples in liquid solutions, this technique may still present an utmost drawback that limits resolution due to slight sample movement between projections. Biological specimens are primarily composed of organic material with a mass density very similar to the medium, that generates a buoyant force comparable with their weight. Consequently, there will be a reduction on the friction force responsible for keeping the sample supported at the sample holder. Therefore, as the friction is the main force responsible for keeping delicate samples still, isopropanol-immersed samples will likely move, especially during sample rotation even though it is very smooth. Besides, biological samples are mostly flexible and non-rigid, being possible to move during data collection, decreasing our rate of success of data collection due to impaired reconstructions.

In order to solve the issue of sample drifting during acquisition, resin- or paraffin-embedded samples were conceptualized as a reasonable solution (Scott *et al.*, 2015). Additionally, resins can also be used, including epoxy or acrylic resins, opening the possibility for multimodal imaging together with transmission electron microscopy (Metscher, 2009; Mizutani & Suzuki, 2012). As can be noticed, the pipeline performed here is a regular procedure used in any histology laboratory, and was shown to be completely compatible with microtomography (Scott *et al.*, 2015; Fonseca *et al.*, 2018).

We observed that paraffin infiltration caused samples to decrease their total length and volume (Fig. 2 and Table 2), and the same reduction was also observed for inner structures such as the eyes and the heart (Figs. 3 and 4; Table 3). However, the volume ratio of the organ volume to the whole sample volume is preserved during the process, guaranteeing that no artifacts are generated during morphologic measurements. Thus, comparative studies between control and test groups are perfectly valid.

Previous studies have already demonstrated such a decrease in volume due to paraffin infiltration (Iwadare *et al.*, 1984; Scott *et al.*, 2015). In a study performed by Bahr and collaborators analyzing over 600 tissue specimens, substantial changes in volume and

weight were observed, and as a rule the weight changes closely in parallel to the volume change (Bahr *et al.*, 1957). However, this decrement is very homogeneous in all the samples analyzed, as we also noticed here. Yet, after exposure to the X-rays, even for multiple tomograms, no changes were observed. Other embedding materials such as gelatin or agar are not recommended, as they are colloidal substances composed of water that would eventually evaporate and lead to sample shrinkage during acquisition. From our experience, adequate sample embedding completely solves the sample movement problem with a 100% success ratio for the presented strategy.

Although several methods can be utilized to dry biological specimens for morphological examinations, critical-point drying, first introduced by Anderson and co-workers, is by far the most widely used (Anderson, 1951). In this method, all the volatile components such as water contained in the sample are replaced with air voids, giving an X-ray image of the remaining constituents. In our case, we critical-point-dried samples that were previously dehydrated with alcohol.

Changes in dimensions of biological tissues due to critical-point drying was previously reported (Kääb *et al.*, 1998). However, when compared with the paraffin-embedded condition, we observed no further alteration either on sample length or volume (Figs. 2–4). It is important to mention that, although a number of microtomographic studies of critical-point-dried samples have already been reported (Happel *et al.*, 2010; van de Kamp *et al.*, 2011; Mizutani *et al.*, 2010), structural distortions can be introduced by this procedure (Small *et al.*, 2008). Also, critical-point-dried samples still rely on gravity and an adequate sample holder geometry for minimizing the sample movement during acquisition (Zysk *et al.*, 2012). Nonetheless, it is still a viable alternative that results in good quality tomograms. It also opens the possibility for multimodal imaging together with scanning electron microscopy.

4.2. Reconstruction and resolution

According to Fig. 5(*a*), it is quite evident that the *z*-slice of the critical-point-dried sample exhibits a better quality than the paraffin-embedded sample, which itself is better than the isopropanol-immersed one.

Firstly, it is worth mentioning that the isopropanol-immersed samples suffer from a chronical sample-drifting problem. Hence, to avoid reconstruction artifacts, the sample is expected to stay still within a range of 0.82 µm, which is our sensitivity to motion (camera pixel size). An optimized acquisition strategy for this kind of sample mounting consists of reducing the exposure time in order to decrease the dose into the isopropanol, therefore avoiding bubbles, and also making the acquisition faster, increasing the chance of success.

The sample movement problem is not observable in the paraffin-embedded larvae and thus resulted in the reconstruction shown in Fig. 5(*a*). As the paraffin held the sample still during the acquisition, it allowed us to set a longer exposure time in order to increase the photon counting by the detector and thus providing a higher accuracy and allowing the perception of more details.

Finally, the critical-point-dried sample, although susceptible to the sample movement problem, was more stable and the acquisition time could also be optimized for photon counting. Still, the slice shown in Fig. 5(*a*) has sharper edges making the image visually better. This effect is attributed to an enhanced phase contrast from the sample. Although the sample-to-detector distance in all three cases is the same, the critical-point-dried sample is free from the surrounding solvent. Thus, the difference in the refractive index between the air and the osmium-impregnated tissue is much higher than for the other two cases, increasing the phase-contrast phenomena (Willmott, 2011), making the edges of the image sharper and thereby visually better.

Isopropanol-immersed larvae have a FSC-calculated resolution of 2.4 µm, compared with 2.6 µm for the paraffin-embedded and the 3.0 µm for the critical-point-dried samples [Fig. 2(*c*)]. This progressive loss in resolution may be attributed to the radiation damage that accumulated in the sample due to the adopted experiment procedure. As the goal of this work was to always measure the same larvae prepared by three consecutive different sample-mounting strategies, the adopted experimental procedure made the paraffin-embedded sample receive twice the X-ray dose, and the critical-point-dried sample receive three times the dose compared with the isoproponal-immersed sample.

In this case, since the FSC correlates the resolution of the entire sample, it will quantify loss in resolution taking all the pixels over the whole volume thus making this metric very sensitive to radiation damage and sample motion. However, the quality of the individual measurements, as presented in the 3D reconstructions and used for the morphoquantitative analyses presented previously, would be almost insensitive to radiation damage as the presented quantitative data would need much higher doses up to the point that it is capable of changing an entire pixel value. Nonetheless, the most significant resolution drop from 2.4 µm to 3.0 µm is smaller than the instrumental pixel size of 0.82 µm that makes the obtained information for all conditions relatively equivalent and does not prejudice the presented morphologial analyses.

5. Conclusion

As a rule, biological tissues have complicated and delicate structures, from the organ level down to the subcellular level. Continuous advances in high-resolution X-ray microtomography have provided us with a practical approach to determining the 3D structures of biological samples at micrometre to submicrometre resolution, offering valuable information on living matter functioning and morphology. In this work, we present a systematic study comparing three distinctive sample-mounting procedures for biologic soft tissues for X-ray µCT. Straightforward approaches such as immersion of samples in pure alcohol, although very practical, have the disadvantage of being very susceptive to sample drifting, limiting the final resolution. Critical-point drying

mitigates this problem, but only paraffin embedding definitively solves the drifting-issue during scanning.

Summarizing, sample mounting is a crucial factor that should be carefully considered when collecting high-resolution and good quality tomograms. Although we observed that all the sample preparation procedures analyzed here alter the original sample morphology, such structural distortions are very homogeneous among samples and between inner and outer structures, thereby allowing comparative analysis in great detail.

Acknowledgements

The authors acknowledge the IMX beamline staff and the Zebrafish Housing Facility at LNLS and LNBio/CNPEM. We also would like to thank Dr Harry Westfahl Jr for carefully reading the manuscript.

Funding information

The following funding is acknowledged: Fundação de Amparo à Pesquisa do Estado de São Paulo (grant No. 2018/20014-0 to MdCF).

References

Amunts, K., Lepage, C., Borgeat, L., Mohlberg, H., Dickscheid, T., Rousseau, M. E., Bludau, S., Bazin, P. L., Lewis, L. B., Oros-Peusquens, A. M., Shah, N. J., Lippert, T., Zilles, K. & Evans, A. C. (2013). *Science*, **340**, 1472–1475.

Anderson, F. T. (1951). *Trans. New York Acad. Sci.* **13**, 130–133.

Andrews, J. C., Almeida, E., van der Meulen, M. C., Alwood, J. S., Lee, C., Liu, Y., Chen, J., Meirer, F., Feser, M., Gelb, J., Rudati, J., Tkachuk, A., Yun, W. & Pianetta, P. (2010). *Microsc. Microanal.* **16**, 327–336.

Bahr, G. F., Bloom, G. & Friberg, U. (1957). *Exp. Cell Res.* **12**, 342–355.

Balint, R., Lowe, T. & Shearer, T. (2016). *PLoS One*, **11**, e0153552.

Bentley, M. D., Jorgensen, S. M., Lerman, L. O., Ritman, E. L. & Romero, J. C. (2007). *Anat. Rec.* **290**, 277–283.

Bonse, U. & Busch, F. (1996). *Prog. Biophys. Mol. Biol.* **65**, 133–169.

Bravin, A., Coan, P. & Suortti, P. (2013). *Phys. Med. Biol.* **58**, R1–R35.

Chen, J. Y., Bottjer, D. J., Li, G., Hadfield, M. G., Gao, F., Cameron, A. R., Zhang, C. Y., Xian, D. C., Tafforeau, P., Liao, X. & Yin, Z. J. (2009). *Proc. Natl Acad. Sci. USA*, **106**, 19056–19060.

Crespigny, A. de, Bou-Reslan, H., Nishimura, M. C., Phillips, H., Carano, R. A. & D'Arceuil, H. E. (2008). *J. Neurosci. Methods*, **171**, 207–213.

Dorr, A. E., Lerch, J. P., Spring, S., Kabani, N. & Henkelman, R. M. (2008). *Neuroimage*, **42**, 60–69.

Fidalgo, G., Colaço, M. V., Nogueira, L. P., Braz, D., Silva, H. R., Colaço, G. & Barroso, R. C. (2018). *J. Instrum.* **13**, C05012.

Fonseca, M. C., Araujo, B. H. S., Dias, C. S. B., Archilha, N. L., Neto, D. P. A., Cavalheiro, E., Westfahl, H. Jr, da Silva, A. J. R. & Franchini, K. G. (2018). *Sci. Rep.* **8**, 12074.

Fusseis, F., Regenauer-Lieb, K., Liu, J., Hough, R. M. & De Carlo, F. (2009). *Nature*, **459**, 974–977.

Happel, C. M., Klose, C., Witton, G., Angrisani, G. L., Wienecke, S., Groos, S., Bach, F. W., Bormann, D., Männer, J. & Yelbuz, T. M. (2010). *Circulation*, **122**, e561–e564.

Heel, M. van & Schatz, M. (2005). *J. Struct. Biol.* **151**, 250–262.

Iwadare, T., Mori, H., Ishiguro, K. & Takeishi, M. (1984). *J. Microsc.* **136**, 323–327.

Johnson, J. T., Hansen, M. S., Wu, I., Healy, L. J., Johnson, C. R., Jones, G. M., Capecchi, M. R. & Keller, C. (2006). *PLoS Genet.* **2**, e61.

Kääb, M. J., Gwynn, I. A. & Nötzli, H. P. (1998). *J. Anat.* **193**(Pt 1), 23–34.

Kak, A. C. & Slaney, M. (1988). *Principles of Computerized Tomographic Imaging.* IEEE Press.

Kamp, T. van de, Vagovič, P., Baumbach, T. & Riedel, A. (2011). *Science*, **333**, 52.

Keyes, S. D., Boardman, M. M., Marchant, A., Roose, T. & Sinclair, I. (2013). *Eur. J. Soil Sci.* **64**, 298–307.

Koshev, N., Elias, S., Helou, Eduardo, X. & Miqueles (2016). *arXiv*: 1608.03589.

Legland, D., Arganda-Carreras, I. & Andrey, P. (2016). *Bioinformatics*, **32**, 3532–3534.

Metscher, B. D. (2009). *Dev. Dyn.* **238**, 632–640.

Mikula, S., Binding, J. & Denk, W. (2012). *Nat. Methods*, **9**, 1198–1201.

Miqueles, E., Koshev, N. & Helou, E. S. (2018). *IEEE Trans. Image Process.* **27**, 894–906.

Miqueles, E. X. & De Pierro, A. R. (2011). *Comput. Phys. Commun.* **182**, 2661–2673.

Mizutani, R. & Suzuki, Y. (2012). *Micron*, **43**, 104–115.

Mizutani, R., Takeuchi, A., Hara, T., Uesugi, K. & Suzuki, Y. (2007). *J. Synchrotron Rad.* **14**, 282–287.

Mizutani, R., Takeuchi, A., Uesugi, K., Ohyama, M., Takekoshi, S., Osamura, R. Y. & Suzuki, Y. (2008). *Brain Res.* **1199**, 53–61.

Mizutani, R., Takeuchi, A., Uesugi, K., Takekoshi, S., Osamura, R. Y. & Suzuki, Y. (2010). *Cereb. Cortex*, **20**, 1739–1748.

Neues, F. & Epple, M. (2008). *Chem. Rev.* **108**, 4734–4741.

Pauwels, E., Van Loo, D., Cornillie, P., Brabant, L. & Van Hoorebeke, L. (2013). *J. Microsc.* **250**, 21–31.

Rodrigues, H. A., Fonseca, M. C., Camargo, W. L., Lima, P. M., Martinelli, P. M., Naves, L. A., Prado, V. F., Prado, M. A. & Guatimosim, C. (2013). *PLoS One*, **8**, e78342.

Ruffins, S. W., Martin, M., Keough, L., Truong, S., Fraser, S. E., Jacobs, R. E. & Lansford, R. (2007). *Sci. World J.* **7**, 592–604.

Salomé, M., Peyrin, F., Cloetens, P., Odet, C., Laval-Jeantet, A. M., Baruchel, J. & Spanne, P. (1999). *Med. Phys.* **26**, 2194–2204.

Scherer, K., Birnbacher, L., Chabior, M., Herzen, J., Mayr, D., Grandl, S., Sztrókay-Gaul, A., Hellerhoff, K., Bamberg, F. & Pfeiffer, F. (2014). *PLoS One*, **9**, e93502.

Scott, A. E., Vasilescu, D. M., Seal, K. A., Keyes, S. D., Mavrogordato, M. N., Hogg, J. C., Sinclair, I., Warner, J. A., Hackett, T. L. & Lackie, P. M. (2015). *PLoS One*, **10**, e0126230.

Shearer, T., Bradley, R. S., Hidalgo-Bastida, L. A., Sherratt, M. J. & Cartmell, S. H. (2016). *J. Cell Sci.* **129**, 2483–2492.

Small, J. V., Auinger, S., Nemethova, M., Koestler, S., Goldie, K. N., Hoenger, A. & Resch, G. P. (2008). *J. Microsc.* **231**, 479–485.

Smith, H. F., Fisher, R. E., Everett, M. L., Thomas, A. D., Randal Bollinger, R. & Parker, W. (2009). *J. Evol. Biol.* **22**, 1984–1999.

Sombke, A., Lipke, E., Michalik, P., Uhl, G. & Harzsch, S. (2015). *J. Comput. Neurol.* **523**, 1281–1295.

Vickerton, P., Jarvis, J. & Jeffery, N. (2013). *J. Anat.* **223**, 185–193.

Wang, H., Zheng, L., Peng, C., Guo, R., Shen, M., Shi, X. & Zhang, G. (2011). *Biomaterials*, **32**, 2979–2988.

Weibel, E. R. & Vidone, R. A. (1961). *Am. Rev. Respir. Dis.* **84**, 856–861.

Willmott, P. R. (2011). *An Introduction to Synchrotron Radiation.* John Wiley and Sons.

Zhu, W., Gaetani, G. A., Fusseis, F., Montesi, L. G. & De Carlo, F. (2011). *Science*, **332**, 88–91.

Zou, W., Hunter, N. & Swain, M. V. (2011). *J. Dent. Res.* **90**, 18–30.

Zysk, A. M., Garson, A. B., Xu, Q., Brey, E. M., Zhou, W., Brankov, J. G., Wernick, M. N., Kuszak, J. R. & Anastasio, M. A. (2012). *Biomed. Opt. Expr.* **3**, 1924–1932.